# Surface Engineering for Molecular Electronics

Qiu, Xinkai

*DOI:*
10.33612/diss.146270150

# 6

# SELF-ASSEMBLED MONOLAYERS OF METAL COORDINATION COMPLEXES ON GOLD SURFACE

Contents of this chapter have been published in *Chem. Commun.* **2019**, 55, 13554-13557. We acknowledged R.Pütt and Prof. dr. K.Y. Monakhov for the synthesis of the compounds and the characterization of their magnetism.

## ABSTRACT

*The two first representatives of phthalocyaninato (Pc) lanthanide-ligated polyoxovanadate cages* $\{[V_{12}O_{32}(Cl)](LnPc)_n\}^{n-5}$ *(n=1 or 2,* $Ln = Yb^{3+}$*) were synthesized and fully characterized. These magnetic complexes form two-dimensional self-assembled monolayers exhibiting electrical conductivity on gold substrate surfaces, as assessed by using an EGaIn tip.*

## 6.1. INTRODUCTION

The possibility of forming stimuli-responsive two-dimensional (2D) monolayers[1] paves the way for implementation of nano-structured molecule-surface interfaces into highly sought-after molecule-based computer memory cells. Self-assembled monolayers (SAMs) consisting of tailor-made metal complexes[2] constitute one of the promising ways of addressing the challenges[3] in the area of molecular electronics (see also **Chapter 1.2** for an introduction on molecular monolayers).[4, 5] To transit to the actual device fabrication, experimentalists need first and foremost to achieve active control of contact-surface impacted single-molecule structure-property stability and of the reproducibility of molecular conductivity measurements. A continuous optimization of coordination compound is furthermore required to eventually minimize resistivity and improve the conductivity of 2D SAMs in the applied electrode environment.

Herein we report on our efforts towards the development of such SAMs whose molecular electronic states can be manipulated on air-stable substrate surfaces by electrical means and their work functions can be tracked by (micro-)spectroscopic methods. Specifically, we elaborate on polyoxovanadates [6] (POVs) and their organic-inorganic hybrid derivatives that have been identified[7] as being able to implement multilevel data storage and processing functions in so-called "More than Moore" information technology (IT) devices. We describe the synthesis, structure and magnetism of $nBu_4N^+$-charged balanced complexes with the general formulas $\{[V_{12}^V O_{32}(Cl)](LnPc)^{4-}\}$ $(mono^{4-})$ and $\{[V_{12}^V O_{32}(Cl)](LnPc)_2\}^{3-}$ $(bis^{3-})$ where Pc is the phthalocyanine dianion (Fig. 6.1). This chapter is a focused case study with $Ln = Yb^{3+}$, emphasising the significance of covalent grafting of late and early lanthanide-Pc moeities onto the lacunary POV core[8, 9] and its far-reaching implications on molecular charge transport characteristics. To the best of our knowledge, the direct interaction between metal-Pc moieties and the polyoxometalate[10, 11] (POM) unit was shown only once. Drain and co-workers synthesized hybrid $(nBu_4N)_5[PW_{11}^{VI}O_{39}(MPc)]$ compounds[12] where the fully-oxidised, lancunary Keggin POM is capped by $MPc^{2+}$ with $M = Zr^{IV}$ or $Hf^{IV}$. Note that there are however plenty of hybrid compounds[13, 14] where the POM unit and the metal-Pc moieties are separated by electrostatic interactions or by an organic linker.



## 6.2. RESULTS AND DISCUSSION

Hybrid $mono^{4-}$ and $bis^{3-}$ were isolated as polycrystalline powders in high yields (95% and 91%) from the reactions of the $(nBu_4N)_4[HV_{12}O_{32}(Cl)]$ precursor with $YbPcOAc \cdot 2MeOH$ (OAc=acetate) in a 1:1 and 1:2.2 ratio in MeCn, respectively (Fig. 6.1). Single-crystal X-ray diffraction studies indicated reactivity-induced changes of the POV building unit from a "closed" to a "tube-like" $V_{12}O_{32}$ structure[15, 16] that is thus capped by one (in $mono^{4-}$) or sandwiched by two (in $bis^{3-}$) $YbPc^+$ moieties. The formal oxidation states of the vanadium and lanthanide atoms were confirmed by bond valence sum calculations $[\sum(V^V) = 4.99 - 5.13, \sum(Yb^{III}) = 2.81]$ for $mono^{4-}$ and $[\sum(V^V) = 4.80 - 5.26, \sum(Yb^{III}) = 2.81]$ for $bis^{3-}$. The formations, compositions and electronic structures of the fully-oxidised $mono^{4-}$ and $bis^{3-}$ are further supported by elemental and thermogravimetric

analyses, electrospray ionisation mass spectrometry and superconducting quantum interference device (SQUID) magnetometry (see Experimental section for details).

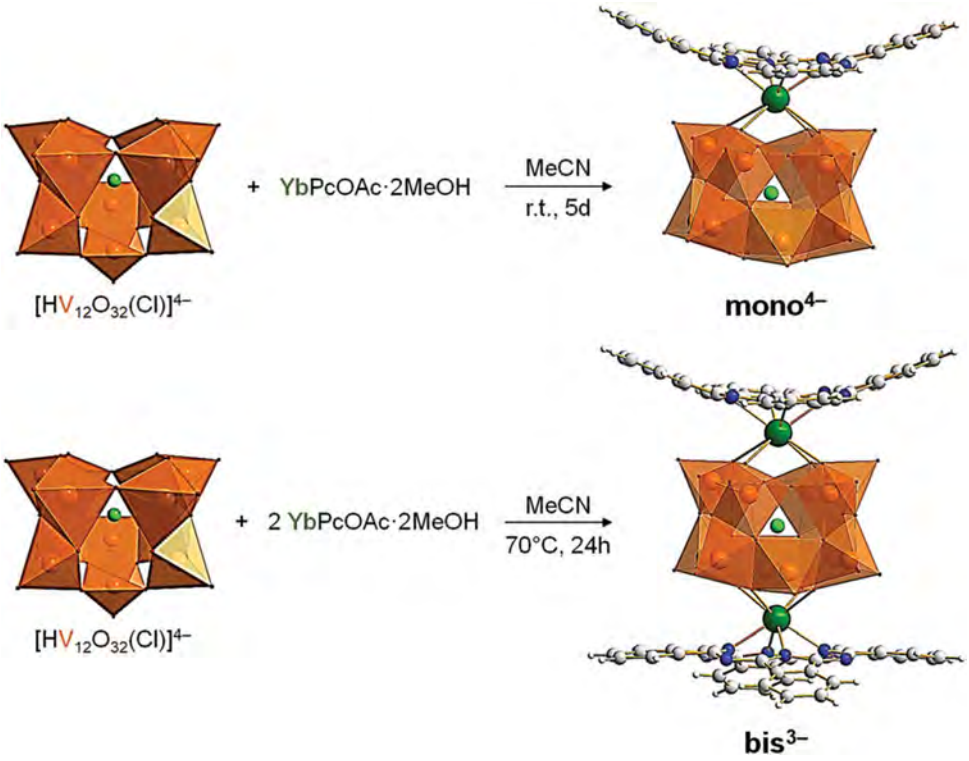


**Figure 6.1 |** Synthesis of fully-oxidized $\{[V_{12}^{V}O_{32}(Cl)](YbPc)_n\}^{n-5}$ hybrid polyanions with $n = 1$ (top, $mono^{4-}$) and $n = 2$ (bottom, $bis^{3-}$). The proton ($H^+$) in $[HV_{12}O_{32}(Cl)]^{4-}$ is not shown. r.t. = room temperature. Color code: Yb = dark green, V = orange polyhedra, Cl = pale green, O = red, N = blue, C = grey, and H = white. See the Experimental section for details.

Magnetism of both compounds arises from $Yb^{3+}$ ions and is dominated by spin-orbit interaction. Because $Yb^{3+}$ has a more than half-filled 4f valence shell, its ground multiplet should correspond to a high total magnetic moment $J = 7/2$.[17] Since the energy gap between the ground and the first exited multiplet in $Yb^{3+}$ is supposed to be around 14000 K[18] only the ground multiplet was considered in modeling of the magnetism. In Fig. 6.2 the molar susceptibility and magnetisation of $mono^{4-}$ are depicted together with theoretical fits. The details of magnetic modelling of $bis^{3-}$ (Fig. 6.10) can be found in the Experimental section.

The electronic structure of $mono^{4-}$ was also assessed by density functional theory calculations (see Experimental section for details) and it is in line with the obtained magnetic data. As illustrated in Fig. 6.3, the negative charge is transferred from the Pc to the POV subunit, while a doublet spin state is strongly localized at the Yb atom. The computed Yb-Cl distance of 4.06 Å matches the experimental value of 4.1001(29) Å determined by X-ray diffraction which is *ca.* 0.34 Å longer than the one in the $bis^{3-}$

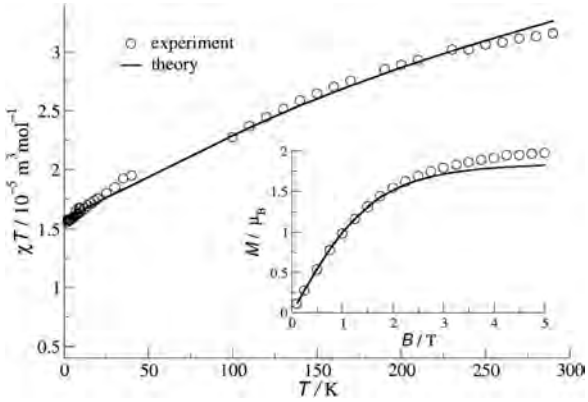


**Figure 6.2 |** Molar susceptibility ($B = 0.1T$) and magnetisation ($T = 2K$) for the polycrystalline powder sample of $mono^{4-}$ (circles) with theoretical fits (solid lines).

derivative (exptl. 3.760(2) Å-3.761(2) Å). This is due to the fact that the Cl atom is pushed away from Yb by *ca.* 0.21 Å in $mono^{4-}$ if the POV center is taken as a reference point. The asymmetry within the POV subunit is induced by the coordinated Yb atom contracting the host-guest vanadium-oxo cluster. The largest O-O distance between the Yb-coordinated oxygen atom is 3.99 Å (exptl. 4.0611(279) Å), and it increases to 4.71 Å (exptl. 4.9368(85) Å) on the opposite POV side for the comparable oxygen atoms.



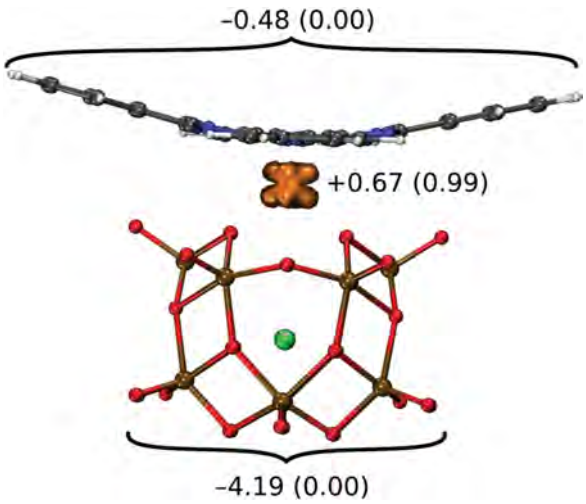


**Figure 6.3 |** Hirshfeld partial charges and regions with increased $\alpha$-spin density (orange isosurface) in $mono^{4-}$. Sum of partial charges is shown without brackets, while the spin density is indicated in brackets.

Next, we succeeded in growing SAMs by immersing freshly cleaved template-stripped[19] gold substrates (atomically smooth $Au^{TS}$) in a 0.1 mM methanolic solution of each tested, thermally stable (up to *ca.* 200 °C coordination compound overnight. The formation of

SAMs is shown in Fig. 6.4a-c. The SAMs were contacted with an eutectic gallium-indium (EGaIn) tip[20] to form tunneling junctions with the structure $Au^{TS}//SAM//Ga_2O_3/EGaIn$, where "/" denotes the interface defined by chemisorption and "//" by physisorption (see also **Chapter 1.3.2** for EGaIn large-area junction). The SAM quality was assessed by measuring the surface morphology of the fabricated samples (Fig. 6.4a-c and Fig. 6.11 in Experimental section) using atomic force microscopy (AFM). The observed particles that correspond to the size of physisorbed $mono^{4-}$ and $bis^{3-}$ are homogeneously distributed over the $Au^{TS}$ substrate (Fig. 6.4a) in comparison to the substrate in the absence of molecular aggregates (Fig. 6.4b). The roughnesses (root mean squared, RMS) of the SAMs are calculated to be 0.417 nm for $mono^{4-}$ and 0.382 nm for $bis^{3-}$. They are thus higher than those obtained from the bare $Au^{TS}$ substrates (0.1 nm), suggesting that the target coordination compounds were successfully immobilized onto the substrates. The formation of monolayers was confirmed by ellipsometric measurements of the SAM thicknesses, resulting in values 0.96±0.07 nm for $mono^{4-}$ and 1.17±0.07 nm for $bis^{3-}$ that are in excellent agreement with the expected height values (*ca.* 0.90 nm *vs.* 1.20 nm) for these hybrid polyoxoanions.

The measured current density-voltage ($J/V$) characteristics of the engineered SAMs are depicted in Fig. 6.4d). Interestingly, the SAM of $bis^{3-}$ exhibits somewhat lower molecular conductivity than $mono^{4-}$ at a lower bias window (from −0.5 V to 0.5 V). However, at a higher bias (*e.g.,* ±1 V) the difference in the rate of tunneling charge transport vanishes, possibly due to the molecular states coming into resonance with the electrode/substrate Fermi level with the increasing bias.[21] Although the magnetism of $mono^{4-}$ and $bis^{3-}$ is dominated by the spin-orbit effects of $Yb^{3+}$ ions, the molecular charge transport characteristics are expected to be strongly influenced by electron transport[22] through the fully-oxidized $V^V$ centers. This is in accordance with our latest results[23] indicating that the Cu(II) center is the main transmission channel across tunneling junctions formed of a series of charge-neutral dinuclear 3d-4f coordination complexes $[CuLn(L\cdot SMe)_2(OOCMe)_2(NO_3)]\cdot xMeOH(Ln = Gd, Tb, Dy and Y; L = Schiff base; x = 0.75-1)$. The latter were similarly immobilized on $Au^{TS}$ in the form of monolayers; however, these SAMs are characterized by lower molecular conductivity compared to the SAMs of $mono^{4-}$ and $bis^{3-}$. In view of these data, further efforts towards the grafting of covalently bound early lanthanide-Pc moieties onto (reduced) POM cores need to be devoted in order to substantially break the energy level alignment of molecular magnetic states with respect to the Fermi level of the applied electrode surfaces.

## 6.3. CONCLUSIONS

The finding described herein offer guidance to customizing a hybrid material that can be assembled of any stable lacunary POM core and phthalocyaninato lanthanide moieties. The structure-directing and structure-stabilising role of the charge-balancing countercations is also worth mentioning.[24] The potential possibilities of controlled fine-tuning of their structural, electrochemical and magnetic characteristics in the applied electrode environment are expected to make 2D monolayers of such POM-based coordination compounds suitable candidates for practical integration into memory cells.[25, 26] To achieve this technology transfer-oriented goal, we will further seek to evoke the SAM

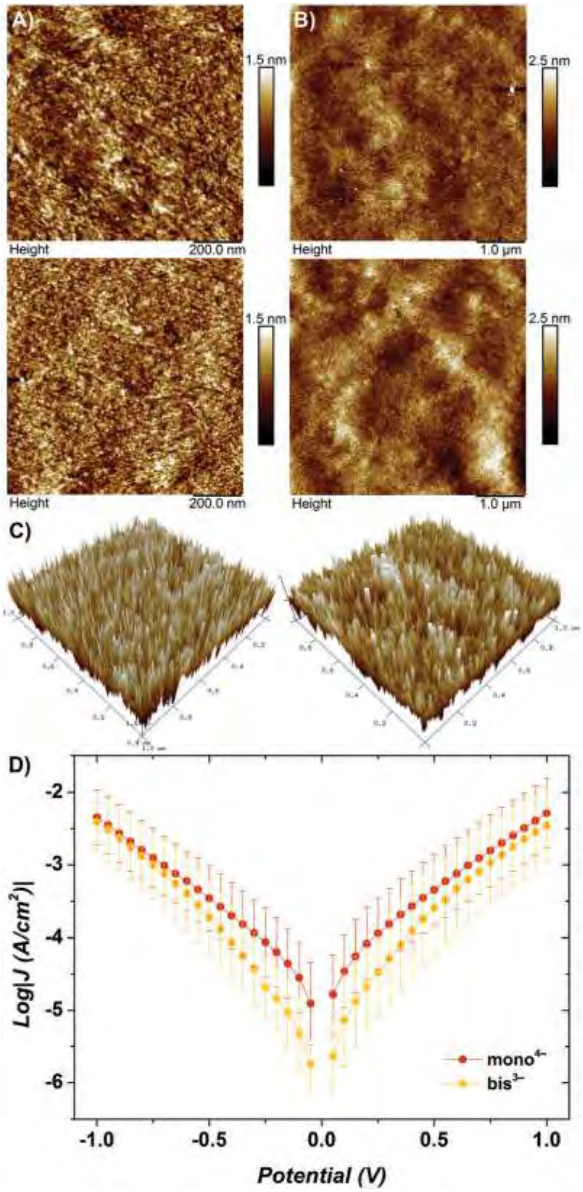


**Figure 6.4 |** AFM height images of SAMs on $Au^{TS}$ (scanned at 500 µm (**a**) and 5 µm (**b**) and the 3D morphology of the sample surfaces (**c**) for $mono^{4-}$ (top/left) and $bis^{3-}$ (bottom/right). **d**, Plots of $log$ current density *vs.* applied bias on the SAMs of $mono^{4-}$ and $bis^{3-}$ on $Au^{TS}$. Values of $\log|J|$ at $V = 0V$ are omitted for clarity. $J = I/A$ where $I$ and $A$ are the current and area of the junction, respectively. Error bars represent the standard deviations of Gaussian fits.

conductivity switching response to the electric field of a scanning probe microscope as a function of oxidation and magnetic states of metal ions or temperature-controlled molecular ordering and/or adsorption geometry in monolayers.

## 6.4. EXPERIMENTAL

### 6.4.1. SYNTHESIS

All starting materials were commercially available and used as received. All solvents were dried over $CaH_2$ and distilled before use. Elemental analysis (carbon, hydrogen and nitrogen, CHN) of compounds was carried out using a Vario EL elemental analyzer.

$(nBu_4N)_4[HV_{12}O_{32}(Cl)]$ was synthesized according to the literature[27] and $YbC_{34}H_{19}O_2N_8 \cdot 2MeOH$ ($C_{32}H_{16}N_8 = Pc$) was synthesized similarly to the protocol reported in the literature[28].

Ytterbium(III) acetate hydrate (2 mmol, calculated on water-free basis) was ground in a mortar and dried for 2 hr in vacuum at 100 °C. After cooling down to room temperature, phthalonitrile (1.55 g, 12 mmol) was added and dried in vacuum at room temperature. Next, dry n−hexanol (15 ml) and dry 1,8−diazabicyclo[5.4.0]undec−7−en (0.9 ml, 6 mmol) were successively added under $N_2$ protection. The suspension was heated up to 160 °C, whereby the suspension gradually cleared up. After a few minutes the color of the solution changed to light green and then to dark green. The reaction was stopped after 30 min, the heating plate was removed and the solution was cooled down to room temperature under ambient conditions. The resulting viscous solution was precipitated into 200 ml of hexane, yielding a nearly black/dark-blue solid. The solid was purified by column chromatography. Using $CH_2Cl_2$ and MeOH in a 99:1 ratio yields the side product $YbPc_2$ (dark green). Using $CH_2Cl_2$ and MeOH in a 95:5 ratio leads to the target product $YbC_{34}H_{19}O_2N_8 \cdot 2MeOH$ (dark blue, 690 mg, 43%).

**Elemental analysis** (%) calcd. for $YbC_{34}H_{19}O_2N_8 \cdot 2MeOH$ ($M = 808.70 g mol^{-1}$): C 53.47, H 3.37, N 13.86; found: C 53.35, H 3.35, N 13.72.

**FT-IR** (KBr, $\tilde{\nu}/cm^{-1}$): 3432 (m), 3086 (w), 2924 (w), 2854 (w), 2231 (w), 1607 (w), 1570 (w), 1525 (vs), 1472 (m), 1455 (m), 1404 (m), 1361 (s), 1324 (s), 1161 (w), 1116 (m), 1081 (w), 1062 (m), 1040 (w), 1019 (w), 965 (w), 886 (w), 839 (w), 768 (s), 730 (vs), 649 (w), 558 (w), 526 (m), 503 (w), 435 (w).

$\{[V_{12}^{V}O_{32}(Cl)](LnPc)\}^{4-}$ ($mono^{4-}$) 106.8 mg (0.05 mmol, 1 eq.) of $(nBu_4N)_4[HV_{12}O_{32}(Cl)]$ and 37.2 mg (0.05 mmol, 1eq.) of $YbPcOAc \cdot 2MeOH$ were dissolved in 5 ml of MeCN using an ultrasonic bath. The solution was allowed to stand for 5 days at room temperature without stirring. The solution was filtered off and the filtrate was dropped into 100 ml of $Et_2O$. The resulting precipitate was centrifuged 10 min in 9000 rpm and washed twice with 40 ml $Et_2O$. The obtained green-blue solid (113 mg, 80%) was dried in vacuum.

**Elemental analysis** (%) calcd. for $(C_{96}H_{160}ClN_{12}O_{32}V_{12}Yb) \cdot Et_2O$ ($M = 2814.36 g mol^{-1}$): C 41.58, H 5.93, N 5.84; found: C 41.45, H 5.98, N 5.43.

**FT-IR** (KBr, $\tilde{\nu}/cm^{-1}$): 3047 (w), 2960 (m), 2933 (m), 2872 (m), 2534 (w), 1634 (w), 1608 (w), 1586 (w), 1564 (w), 1483 (s), 1458 (m), 1407 (w), 1380 (w), 1329 (s), 1282 (m), 1159 (w), 1112 (s), 1078 (m), 1061 (s), 994 (vs), 886 (m), 827 (m), 767 (m), 743 (s), 733 (vs), 681 (s),

630 (m).

**UV-vis** (MeCN, $\lambda/nm$): 222, 240, 337, 608, 644, 674.

**ESI-MS** (MeCN, $m/z$): $[M+6Bu_4N+H]^{2+}$ *calcd.* 1649.47, *exptl.* 1649.46; $[M+5Bu_4N+H]^{+}$ *calcd.* 3056.65, *exptl.* 3056.63; $[M+2Bu_4N+H]^{2-}$ *calcd.* 1164.90, *exptl.* 1164.90; $[M+Bu_4N+H]^{-}$ *calcd.* 2329.80, *exptl.* 2329.81; where $M = V_{12}O_{32}ClYbC_{32}H_{16}N_8$.

$[V_{12}^{V}O_{32}(Cl)](LnPc)_2{}^{3-}$ ($bis^{3-}$) 75 mg (0.035 mmol, 1 eq.) of $(nBu_4N)_4[HV_{12}O_{32}(Cl)]$ and 62.7 mg (0.078 mmol, 2.2 eq.) of $YbPcOAc\cdot 2MeOH$ were dissolved in 5 ml of MeCN using an ultrasonic bath. The solution was allowed to stand for 2 days without stirring at 70 °C. After cooling down to room temperature, the solution was filtered off and the filtrate was dropped into 100 ml of $Et_2O$. The resulting precipitate was centrifuged and washed two times with 40 ml of $Et_2O$. The obtained blue solid (111 mg, 91%) was dried in vacuum.

**Elemental analysis** (%) calcd. for $(C_{112}H_{140}ClN_{19}O_{32}V_{12}Yb_2)\cdot 4Et_2O$ ($M = 3552.46 g mol^{-1}$): C 43.26, H 5.11, N 7.49; found: C 43.10, H 5.13, N 7.29.

**FT-IR** (KBr, $\tilde{\nu}/cm^{-1}$): 3047 (w), 2960 (m), 2931 (m), 2872 (m), 2534 (w), 1633 (w), 1607 (w), 1586 (w), 1563 (w), 1484 (s), 1457 (m), 1407 (w), 1379 (w), 1329 (s), 1281 (m), 1159 (w), 1112 (s), 1078 (m), 1061 (s), 995 (vs), 886 (m), 810 (m), 770 (m), 743 (s), 732 (vs), 676 (m), 629 (m), 614 (m).

**UV-vis** (MeCN, $\lambda/nm$): 222, 240,336, 608, 642, 671.

**ESI-MS** (MeCN, $m/z$): $[M+5Bu_4N]^{+}$ *calcd.* 3741.73, *exptl.* 3741.70; $[M+6Bu_4N]^{2+}$ *calcd.* 1992.01, *exptl.* 1992.0; $[M+2Bu_4N]^{2-}$ *calcd.* 1507.44, *exptl.* 1507.43; $[M+Bu_4N]^{2-}$ *calcd.* 1386.30, *exptl.* 1386.31; where $M = V_{12}O_{32}ClYb_2C_{64}H_{32}N_{16}$.



### 6.4.2. INFRARED SPECTROSCOPY

IR spectra were recored on a Nicolet Avatar 360 FT-IR spectrometer by using KBr pellets ($m_{KBr} \approx 250 mg$) in the 4000-400 $cm^{-1}$ range.

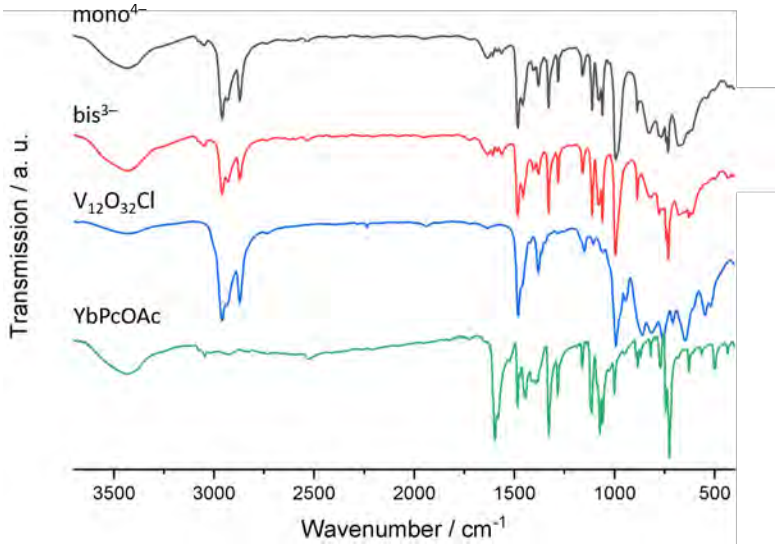


**Figure 6.5 |** A comparison of IR spectra of $mono^{4-}$, $bis^{3-}$, $(nBu_4N)_4[HV_{12}O_{32}(Cl)]$ (abbreviated as $V_{12}O_{32}Cl$) and $YbPcOAc \cdot 2MeOH$ (abbreviated as $YbPcOAc$).

6

### 6.4.3. UV-VIS SPECTROSCOPY

UV-vis spectra were recorded on a Shimadzu UV-2600 spectrophotometer. The samples were dissolved in dry acetonitrile and measured in quartz cuvettes ($d = 1cm$).

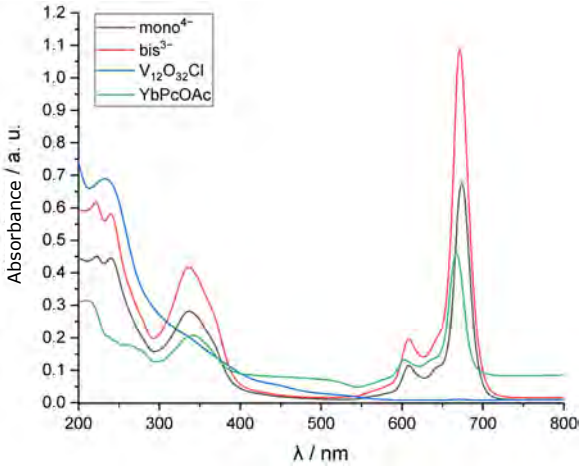


**Figure 6.6 |** A comparison of UV-vis spectra of $mono^{4-}$ ($c = 4 \times 10^{-6}$), $bis^{3-}$ ($c = 4 \times 10^{-6}$), $(nBu_4N)_4[HV_{12}O_{32}(Cl)]$ (abbreviated as $V_{12}O_{32}Cl$; $c = 1.2 \times 10^{-5}$) and $YbPcOAc \cdot 2MeOH$ (abbreviated as $YbPcOAc$; $c = 2 \times 10^{-5}$). All measurements were performed in MeCN.

### 6.4.4. MASS SPECTROMETRY

The ESI-MS spectra were recorded in the positive and negative ion modes using a 4000 QTRAP mass spectrometer system.

**Table 6.1 |** Experimental and calculated *m/z* values for different fragments of $mono^{4-}$.

| Fragment ion | *m/z* exptl. | *m/z* calcd. |
|---|---|---|
| $[(Bu_4N)_5[HV_{12}O_{32}Cl]Yb(Pc)]^+$ | 3056.63 | 3056.65 |
| $[(Bu_4N)_4[HV_{12}O_{32}Cl]Yb(Pc)]^+$ | 2814.15 | 2814.37 |
| $[(Bu_4N)_6[HV_{12}O_{32}Cl]Yb(Pc)]^{2+}$ | 1649.46 | 1649.47 |
| $[(Bu_4N)_3[HV_{12}O_{32}Cl]Yb(Pc)]^-$ | 2572.09 | 2572.08 |
| $[(Bu_4N)_2[HV_{12}O_{32}Cl]Yb(Pc)]^-$ | 2329.81 | 2329.80 |
| $[(Bu_4N)_2[HV_{12}O_{32}Cl]Yb(Pc)]^{2-}$ | 1164.90 | 1164.90 |

### 6.4.5. MOLECULAR AND CRYSTAL STRUCTURES

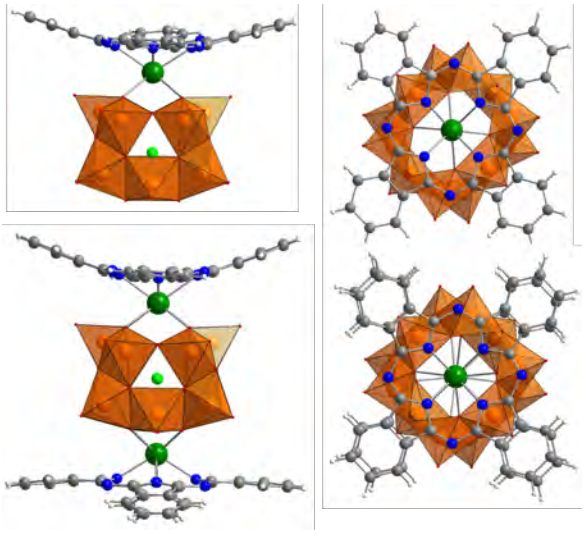

**Figure 6.7 |** Molecular structures of $mono^{4-}$ (top) and $bis^{3-}$ (bottom).



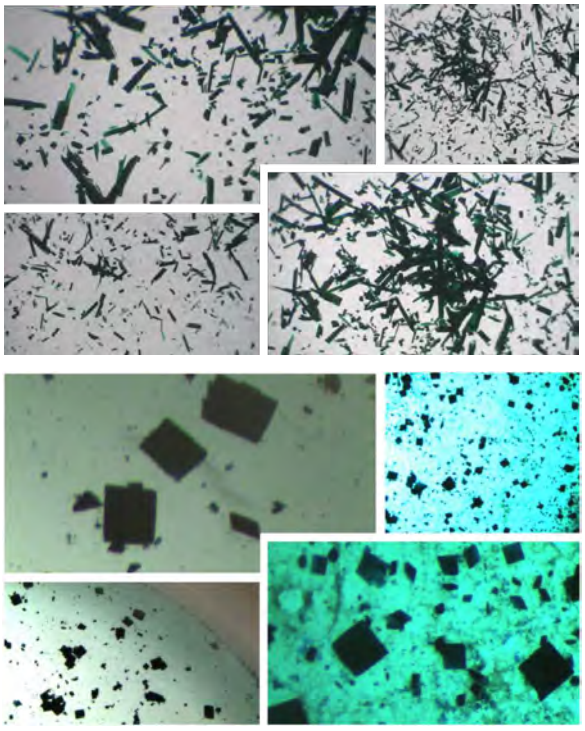

**Figure 6.8 |** Photographs of characteristic needle-shaped crystals of $mono^{4-}$ (top) and square-shaped crystals of $bis^{3-}$ (bottom).

### 6.4.6. THERMOGRAVIMETRIC ANALYSIS

Thermogravimetric analysis was performed with a Mettler-Toledo TGA/SDTA 851e in $N_2$ atmosphere and air with a heating rate of $10 K min^{-1}$.

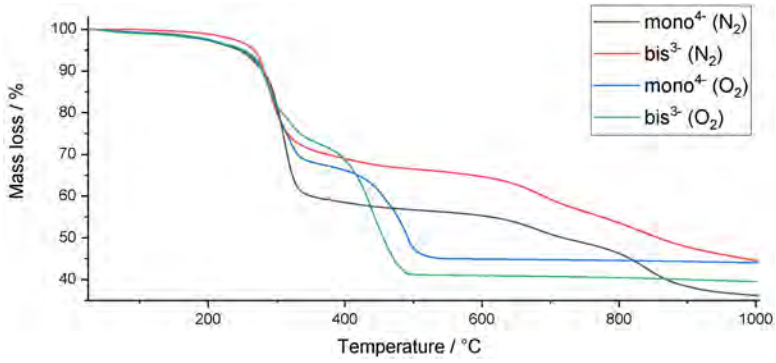


**Figure 6.9 |** TGA curves of $mono^{4-}$ and $bis^{3-}$ measured under nitrogen atmosphere and in dry air.

### 6.4.7. MAGNETOCHEMICAL ANALYSIS

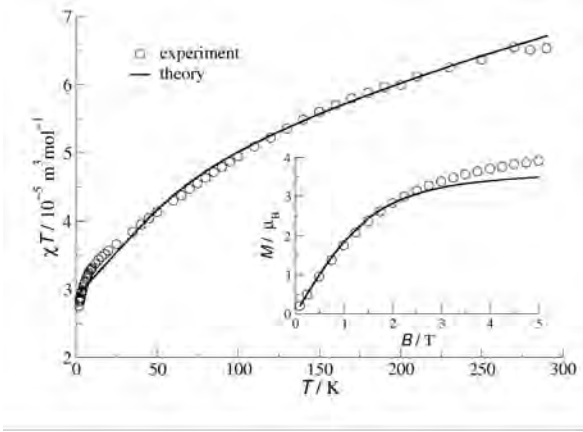


**Figure 6.10 |** Molar susceptibility ($B = 0.1\,T$) and magnetisation ($T = 2K$) for polycrystalline powder sample of $bis^{3-}$ (circles) with theoretical fits (solid lines).

### 6.4.8. EGAIN MEASUREMENTS

The electrical measurement with EGaIn was performed under ambient conditions. In the measurement, the sample was grounded and the EGaIn was biased. At least three samples were examined for SAMs of $mono^{4-}$ and $bis^{3-}$. The potential windows included the following: $0\,V \rightarrow 1\,V \rightarrow -1\,V \rightarrow 0\,V$, steps of 0.05 V. A total of 5 trace/retrace cycles

were recorded for each junctions, and shorts occurred during the measurement (short upon contact with a bias of 1 V or during the cycle) were counted for a failure of junction.

### 6.4.9. ATOMIC FORCE MICROSCOPY

PeakForce Tapping AFM and PFQNM AFM measurements were performed on a Bruker AFM multimode MMAFM-2 model. Pure SAMs of $mono^{4-}$ and $bis^{3-}$ were characterized by AFM on both morphology and surface adhesion. PeakForce Tapping AFM was performed with a ScanAsyst-Air probe (resonant frequenct 70 kHz, spring constant 0.4 N/m, Bruker) to characterize the surface morphology of the samples at a scan rate of 0.7 Hz and 768 samples per line. The data were analyzed with Nanoscope Analysis 1.5 provided by Bruker. Measurements of adhesion were performed in the PFQNM mode. The samples were contacted with a silicon nitride tip with a nominal radius of 1 nm (SAA-HPI-SS, Bruker, resonant frequency 55 kHz, spring constant 0.25 N/m). The deflection sensitivity, spring constant of the cantilever and tip radius were calibrated both before and after the measurement. Samples were scanned at 1 µm and 500 µm at a rate of 0.7 Hz and 640 samples per line. Adhesion of the samples were measured under a force load of 0.3 nN.



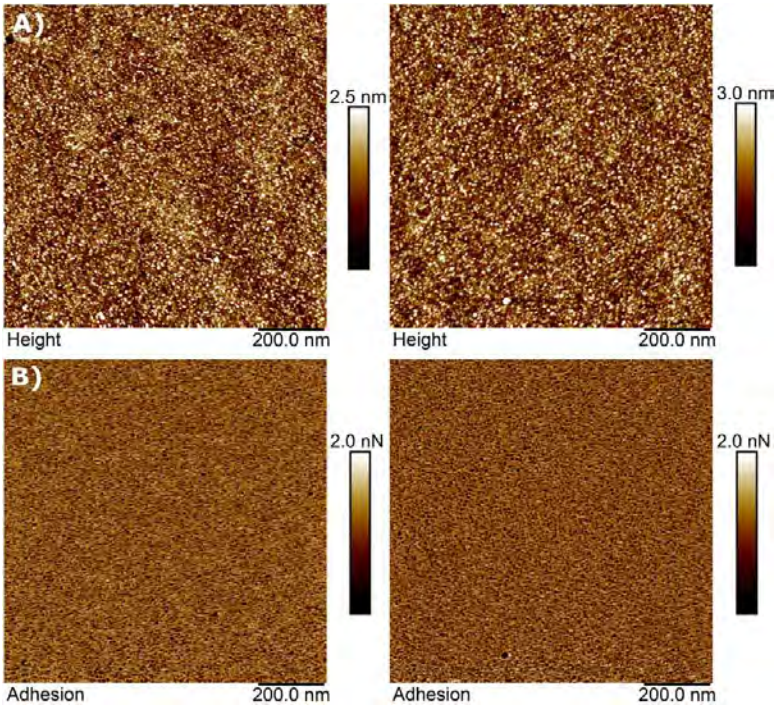


**Figure 6.11 |** AFM height (**a**) and adhesion (**b**) images of SAMs of $mono^{4-}$ (left) and $bis^{3-}$ (right) on $Au^{TS}$ scanned at 1 µm. The interaction between the AFM tip and the Au substrate results in stronger adhesion, while the complexes exhibit weaker adhesion to the tip and appear as dark spots in the image.

### 6.4.10. ELLIPSOMETRY

The ellipsometry measurements were carried out in air, on a V-Vase Rotating Analyzer equipped with a HS-190 monochromator ellipsometer from J.A. Woollam Co., Inc., at an incident angle of 65°, 70° and 75° with respect to the surface normal. A two-layer model consisting of a bottom Au layer, for which optical constants were calculated from freshly prepared template-stripped Au surfaces, and a Cauchy layer was used for the fit of the measurement on the SAMs. A chosen value of $A_n = 1.45$, $B_n = C_n = 0$ and $k = 0.01$ at all wavelengths was used to fit the thickness. For every SAM, we measured six different spots in total (either two spots per sample for three samples or three spots per sample for two samples were measured) and report the thicknesses as the average with the standard deviation as the error bars.

## REFERENCES

[1] Y. Yao, L. Zhang, E. Orgiu, and P. Samorì, *Unconventional nanofabrication for supramolecular electronics,* Adv. Mater. **31**, 1 (2019).

[2] S. J. Higgins and R. J. Nichols, *Metal/molecule/metal junction studies of organometallic and coordination complexes; What can transition metals do for molecular electronics?* Polyhedron **140**, 25 (2018).

[3] D. Xiang, X. Wang, C. Jia, T. Lee, and X. Guo, *Molecular-scale electronics: from concept to function,* Chem. Rev. **116**, 4318 (2016).

[4] L. Vilà-Nadal, S. G. Mitchell, S. Markov, C. Busche, V. Georgiev, A. Asenov, and L. Cronin, *Towards polyoxometalate-cluster-based nano-electronics,* Chem. Eur. J. **19**, 16502 (2013).

[5] C. Busche, L. Vilà-Nadal, J. Yan, H. N. Miras, D. L. Long, V. P. Georgiev, A. Asenov, R. H. Pedersen, N. Gadegaard, M. M. Mirza, D. J. Paul, J. M. Poblet, and L. Cronin, *Design and fabrication of memory devices based on nanoscale polyoxometalate clusters,* Nature **515**, 545 (2014).

[6] M. Stuckart and K. Y. Monakhov, *Vanadium: polyoxometalate chemistry in Encyclopedia of inorganic and bioinorganic chemistry* (2018) pp. 1–19.

[7] O. Linnenberg, M. Moors, A. Notario-Estévez, X. López, C. De Graaf, S. Peter, C. Baeumer, R. Waser, and K. Y. Monakhov, *Addressing multiple resistive states of polyoxovanadates: conductivity as a function of individual molecular redox states,* J. Am. Chem. Soc. **140**, 16635 (2018).

[8] Y. Hayashi, *Hetero and lacunary polyoxovanadate chemistry: Synthesis, reactivity and structural aspects,* Coord. Chem. Rev. **255**, 2270 (2011).

[9] J. M. Cameron, G. N. Newton, C. Busche, D. L. Long, H. Oshio, and L. Cronin, *Synthesis and characterisation of a lanthanide-capped dodecavanadate cage,* Chem. Commun. **49**, 3395 (2013).

[10] D. L. Long, R. Tsunashima, and L. Cronin, *Polyoxometalates: building blocks for functional nanoscale systems,* Angew. Chem. Int. Ed. **49**, 1736 (2010).

[11] M. Stuckart and K. Y. Monakhov, *Polyoxometalates as components of supramolecular assemblies,* Chem. Sci. **10**, 4364 (2019).

[12] I. Radivojevic, K. Ithisuphalap, B. P. Burton-Pye, R. Saleh, L. C. Francesconi, and C. M. Drain, *Ternary phthalocyanato Hf(iv) and Zr(iv) polyoxometalate complexes,* RSC Adv. **3**, 2174 (2013).

[13] Y. Yang, L. Xu, F. Li, X. Du, and Z. Sun, *Enhanced photovoltaic response by incorporating polyoxometalate into a phthalocyanine-sensitized electrode,* J. Mater. Chem. **20**, 10835 (2010).

[14] X. Song, R. Liu, Z. Sun, H. Shi, and L. Xu, *Polyoxometalates as electron-transport materials in phthalocyanine-sensitized solar cells,* Mater. Res. Bull. **97**, 326 (2018).

[15] Y. Inoue, Y. Kikukawa, S. Kuwajima, and Y. Hayashi, *A chloride capturing system: Via proton-induced structure transformation between opened- and closed-forms of dodecavanadates,* Dalton Trans. **45**, 7563 (2016).

[16] S. Kuwajima, Y. Ikinobu, D. Watanabe, Y. Kikukawa, Y. Hayashi, and A. Yagasaki, *A Bowl-Type Dodecavanadate as a Halide Receptor,* ACS Omega **2**, 268 (2017).

[17] J. Jensen and A. R. Mackintosh, *Rare earth magnetism* (Clarendon Press, Oxford, 1991) p. 413.

[18] G. H. Dieke, *Spectra and energy levels of rare earth ions in crystals* (Wiley, New York, 1968).

[19] E. A. Weiss, G. K. Kaufman, J. K. Kriebel, Z. Li, R. Schalek, and G. M. Whitesides, *Si/SiO2-templated formation of ultraflat metal surfaces on glass, polymer, and solder supports: Their use as substrates for self-assembled monolayers,* Langmuir **23**, 9686 (2007).

[20] R. C. Chiechi, E. A. Weiss, M. D. Dickey, and G. M. Whitesides, *Eutectic gallium–indium (EGaIn): a moldable liquid metal for electrical characterization of self-assembled monolayers,* Angew. Chem. Int. Ed. **47**, 142 (2008).

[21] Y. Zhang, S. Soni, T. L. Krijger, P. Gordiichuk, X. Qiu, G. Ye, H. T. Jonkman, A. Herrmann, K. Zojer, E. Zojer, and R. C. Chiechi, *Tunneling probability increases with distance in junctions comprising self-assembled monolayers of oligothiophenes,* J. Am. Chem. Soc. **140**, 15048 (2018).

[22] M. Laurans, K. Dalla Francesca, F. Volatron, G. Izzet, D. Guerin, D. Vuillaume, S. Lenfant, and A. Proust, *Molecular signature of polyoxometalates in electron transport of silicon-based molecular junctions,* Nanoscale **10**, 17156 (2018).

[23] S. Schmitz, A. Kovalchuk, A. Martín-Rodríguez, J. Van Leusen, N. V. Izarova, S. D. Bourone, Y. Ai, E. Ruiz, R. C. Chiechi, P. Kögerler, and K. Y. Monakhov, *Element-selective molecular charge transport characteristics of binuclear copper(II)-lanthanide(III) complexes,* Inorg. Chem. **57**, 9274 (2018).

[24] A. Misra, K. Kozma, C. Streb, and M. Nyman, *Beyond charge balance: counter-cations in polyoxometalate chemistry,* Angew. Chem. Int. Ed. **59**, 596 (2020).

[25] R. van Eldik and L. Cronin, *Polyoxometalate chemistry*, Vol. 69 (Elsevier, Amsterdam, 2017).

[26] X. Chen, Y. Zhou, V. A. Roy, and S. T. Han, *Evolutionary metal oxide clusters for novel applications: toward high-density data storage in nonvolatile memories,* Adv. Mater. **30**, 1 (2018).

[27] K. Okaya, T. Kobayashi, Y. Koyama, Y. Hayashi, and K. Isobe, *Formation of $V^V$ lacunary polyoxovanadates and interconversion reactions of dodecavanadate species,* Eur. J. Inorg. Chem. , 5156 (2009).

[28] M. Bouvet, P. Bassoul, and J. Simon, *Synthesis and electrical properties of a new molecular semiconductor: The uns ymme trical lutetium phthalo-naphthalocyanine,* Mol. Cryst. Liq. Cryst. **252**, 31 (1994).